Full Paper

Israel Journal of Chemistry

DOI: 10.1002/ijch.201900156

Relationship between Phase Fractions and Mechanical Properties in Heat-Treated Laser Powder-Bed Fused Co-Based Dental Alloys

Jonas von Kobylinski,*[a] Leonhard Hitzler,[a] Robert Lawitzki,[b] Christian Krempaszky,[a] Andreas Öchsner,[c] and Ewald Werner[a]

Abstract: Metal additive manufacturing of dental prostheses consisting of cobalt–chromium–tungsten (Co–Cr–W) alloys poses an alternative to investment casting. However, metal additive manufacturing processes like Laser Powder-Bed Fusion (LPBF) can impact the elastic constants and the mechanical anisotropy of the resulting material. To investigate the phase compositions of mechanically different specimens in dependence of their postprocessing steps (e.g. heat treatment to relieve stress), the current study uses X-ray Diffraction (XRD), Electron BackScatter Diffraction (EBSD), and Transmission Electron Microscopy (TEM) for phase identification. Our studies connect plastic deformation of Remanium star CL alloy with the formation of the hexagonal ε-phase and heat treatment with the formation of the D024-phase, while partially explaining previously observed differences in Young's moduli.

Keywords: Co–Cr–W · phase transformation · additive manufacturing · elastic anisotropy · dental restorations · LPBF

1. Introduction

1.1 Motivation

Additive manufacturing (AM) technologies have underwent an immense development in the last decade and nowadays facilitate the fabrication of directly deployable components.[1,2] Out of all these various technologies, those within the category of powder-bed fusion (PBF), specified in the international standard ISO/ASTM 52900:2015,[3] are the ones with the highest relevance for the fabrication of metallic components for clinical purposes.[4–6] These include techniques like electron beam melting (EBM), LPBF and several others.[1] In the scope of dental purposes, the LPBF process, incorporating full melting of the raw material, represents the most relevant process, utilizing a highly focused laser beam as primary energy source with correspondingly small melt pools, favorable for fine surface textures and delicate structures.[7] In addition, it offers significant benefits in terms of overall processing time and predictable clinical outcomes.[8–13] Since design and manufacture are digitally controlled, the devices are likely to be much closer to the manufacturer's specification than those produced by investment casting, which is fraught with many variations and often requires exceptional manual dexterity to minimise potential errors.[14] Nevertheless, metallic components fabricated in a layer-based fashion are likely to display substantial anisotropic material behaviour, necessitating thorough understanding of the underlying microstructure formation, which causes the macroscopic anisotropy.[15–17] Currently, there is a gap in knowledge concerning a comprehensive description of the relationship between the microstructure and the resulting mechanical properties of additively processed dental grade Cobalt–Chromium (CoCr) alloys, as well as their response to post heat treatments. Most major suppliers for dental LPBF printers recommend a post heat treatment procedure for their dental CoCr alloys to enhance their properties. However, even without these, dental restorations, such as crowns, are likely to undergo a ceramic firing to add a porcelain finish for improved aesthetics.[18,19] Recent studies evaluating the mechanical properties of LPBF processed CoCr in the as-fabricated and the heat treated conditions, returned inconclusive results. Foremost, the significant increase of the elastic stiffness (Young's modulus) noted in several heat treated conditions, compared to the low Young's modulus in the as-built condition, barely meets the ISO 22674:2016 standard. This standard requires at least

[a] *J. von Kobylinski, L. Hitzler, C. Krempaszky, E. Werner*
Institute of Materials Science and Mechanics of Materials, Technical University of Munich, Boltzmannstr. 15, 85748 Garching, Germany
E-mail: woste@wkm.mw.tum.de
[b] *R. Lawitzki*
Institute of Materials Science, Chair of Materials Physics, University of Stuttgart, Heisenbergstr. 3, 70569 Stuttgart, Germany
[c] *A. Öchsner*
Faculty of Mechanical Engineering, Esslingen University of Applied Sciences, Kanalstraße 33, 73728 Esslingen, Germany

150 GPa, which is a rather low Young's modulus compared to the conventionally fabricated bulk CoCr.[20] The first assumption to explain these findings resides on the different crystallographic structures being present in either condition: predominantly face centered cubic (fcc; γ-Co) in the as-fabricated condition; and hexagonal close packed (hcp; ε-Co) in the heat treated condition. However, according to Kajima et al.[21] γ-Co remains the predominant phase in all instances, with declining volume fractions of ε-Co with increasing heat treatment temperatures. Given this holds true, there have to be additional factors for the approximate raise of 40–50 GPa in Young's modulus, which this study aims to describe. The theoretical study of the thermodynamical equilibrium by Yang et al.[22] predicts the existence of several phases in addition to the γ and the ε- phases: the σ- and μ- phases and a phase with Co_3W-stoichiometry. To shed light on this, dental grade Co–Cr–W samples were investigated via XRD and electron microscopy in their as-fabricated and heat treated state both prior and after plastic deformation. Moreover, the stress induced phase change from γ-Co to ε-Co was studied on ruptured samples.

2. Methodology

2.1 Sample Preparation

The specimens were supplied by Objective 3D (Australia) as 7 mm × 55 mm cylindrical bars built in an Mlab printer (Concept Laser GmbH, Germany). Samples were built from the dental grade Remanium star CL alloy (Dentaurum GmbH & Co. KG, Germany) with the following chemical composition: 28 Cr, 9W, 1.5Si,. . ., bal. Co (in weight %).[16] In order to capture anisotropy and its response to post heat treatment, samples with the polar angles 0°, 30°, 60° and 90° in the as-fabricated and heat treated condition were evaluated. Heat-treatment was completed by the supplier in an argon atmosphere using a heating rate of 400 K/hour to 1150 °C followed by a 1 h dwell time before furnace cooling to 300 °C.[19] This particular treatment is recommended by Concept Laser for the Co–Cr–W alloy used for dental applications.

2.2 Metallography

Four grinding and mechanical polishing steps were performed to expose the microstructure of the material. The steps comprised grinding with silicon carbide (SiC) 220 grid sandpaper, polishing with 9 µm and 3 µm diamond suspension and surface finishing with a silicon monoxide (SiO) solution with a particle size of 0.5 µm. The visibility of the scan track pattern and the inherent grain structure was enhanced by a subsequent electrochemical etching at 3 V for 10 seconds in a 3 % hydrochloric acid solution. High-resolution images of the etched micro-sections were taken with an optical light microscope (Axio Imager z2 m, Carl Zeiss Microscopy GmbH, Jena, Germany).

2.3 Tensile Testing

Tensile testing was performed as per ISO 22674 : 2016 test guidelines[23] on three samples of each condition (inclination and heat treatment condition) by subjecting them to uniaxial tensile loading until failure. Machined specimens (gauge diameter 3 mm, gauge length 15 mm, radial shoulders) were tested at a constant crosshead speed of 1.5 mm/min in an Instron 5584 tensile testing machine equipped with a 10 kN load cell and a video extensometer of type 2663–821 (Instron Corp., Norwood, MA, USA).[20] Applied nomenclature for the tensile properties is in accordance with DIN EN ISO 6892–1 : 2009.[24]

2.4 XRD

XRD studies for phase identification were performed on four differently configured Co–Cr–W samples: as built, heat treated, deformed and heat treated & deformed. Specimens for XRD had their axis oriented 60° w.r.t. the substrate plate. Diffraction was performed using Cu–Kα on a Bruker Discover instrument featuring a graphite monochromator and a VÅNTEC-2000 two-dimensional detector. For the deformed tensile specimens, it was deemed necessary to accumulate the results of three different section orientations (sectioned with electrical discharge machining) for further reduction of the influence of texture on the resulting diffractograms, see Figure 1. All specimens were ground and then polished with 6 µm diamond polish. In order to be less susceptible to grain statistics, the samples were oscillated (resulting in a minimum effective sample volume of 3 mm × 0.5 mm) and rotated around their plane normal during the measurements for spatial and directional averaging.

2.5 Focused Ion Beam and Scanning Electron Microscopy (FIBSEM)

Prior to EBSD measurements, grinding with 4000 grid SiC paper and electropolishing with an H3PO4-electrolyte were performed. A dual beam FEI SCIOS FIBSEM equipped with an EDAX EBSD system was used for EBSD measurements, followed by data analysis with the TEAM software. Energy-Dispersive X-ray Spectroscopy (EDS) measurements were performed on specimens in the heat treated condition.

2.6 TEM

TEM sample preparations were carried out on one heat treated specimen, using the aforementioned FIBSEM via standard lift

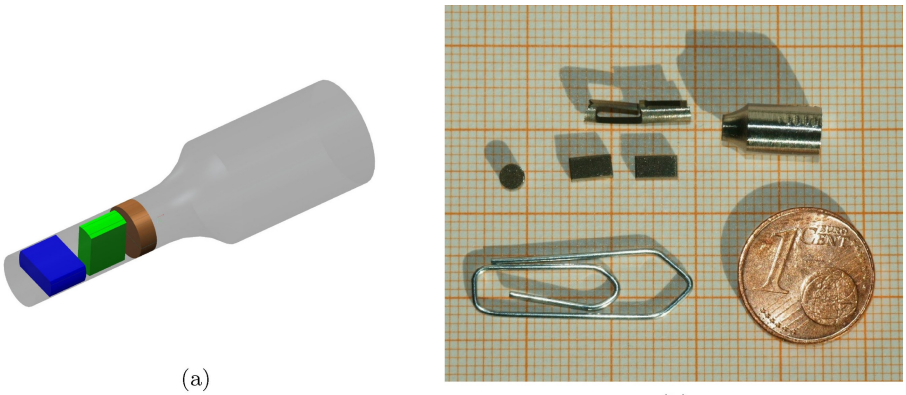

(a) (b)

Figure 1. Post mortem sample preparation of tensile specimens for XRD measurements. 1a: Schematic, 1b: Photographic view. The coin and paper clip are shown for reference.

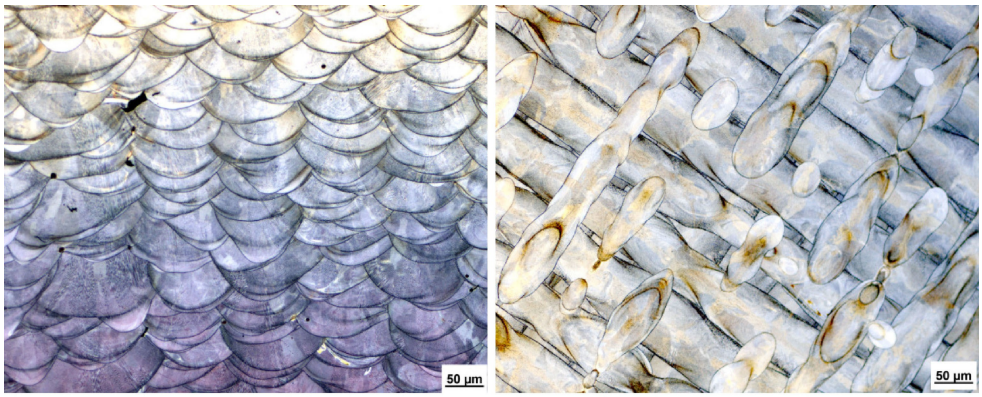

(a) (b)

Figure 2. Microsections of the as-built state. The weld-bead structures are clearly visible, while the section perpendicular to the build direction shows minor amounts of pores. 2a: Microsection parallel to the build direction. 2b: Microsection perpendicular to the build direction. Images reproduced from [20].

out procedure. Measurements were performed with a Philips CM-200 FEG TEM. EDS maps were created using STEM-mode to determine the chemical compositions of matrix and precipitates. For phase identification, diffraction patterns of four precipitates tilted into different random, low indexed zone axes were taken by illumination of areas within the precipitates. Herefore, a small C2 aperture of 30 µm in diameter was used and the diffraction lens was adjusted accordingly. Diffraction patterns were created with the software JEMS[25] and fitted to the data with the software Crystbox.

3. Results

3.1 Metallography

In the as-built condition the appearance of the microstructure was goverened by the weld-bead structure, resembling the applied scanning strategy with the 90° alternation between consecutive layers. The recrystallization during the heat treatment reduced the visibility of this interlaced pattern significantly, see Figures 2 and 3 for the corresponding micrographs.

3.2 Tensile Properties

The mechanical characterisation via tensile testing has been subject of an earlier study, to which the reader is referred to for a greater coverage of this topic[20][1]. Hereafter, only the important findings relevant for the current study are covered. In Table 1 the results from the as-built condition are summarized and Table 2 contains the equivalent data for the heat treated condition. Typical stress-strain diagrams are depicted in Figure 4(a). Despite the typically large dislocation densities after the LPBF process,[26] significant work hardening was observed in the as-built condition.

[1] open access

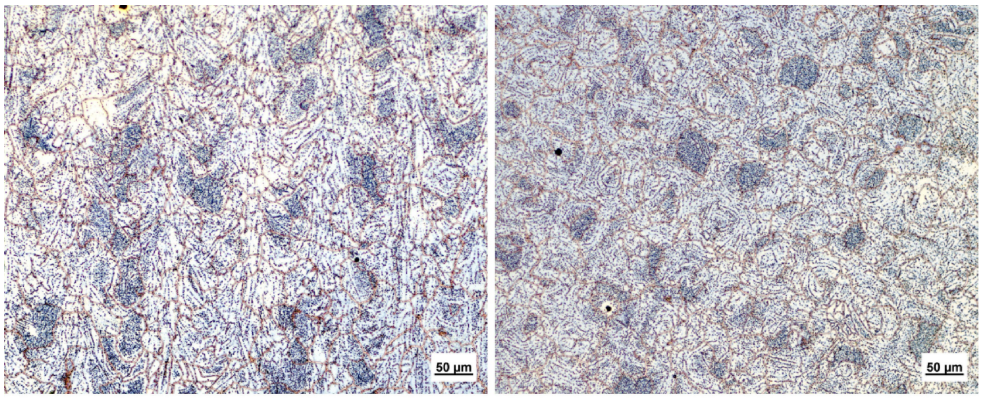

(a) (b)

Figure 3. Microsections of the heat treated state. Due to recrystallization, the weld-bead structures are less visible. The regularly spaced discolorations suggest that the segregations were influenced by the scanning strategy (pattern). 3a: Microsection parallel to the build direction. 3b: Microsection perpendicular to the build direction. Images reproduced from [20].

Table 1. Tensile properties of Co–Cr–W in the as-fabricated condition; extracted from [20]. Φ : Inclination, *E*: Young's modulus, *Rp*0.2: Yield strength, *Rm*: Ultimate tensile strength, *At*: Elongation at failure.

Φ [°]	*E* [GPa]	*Rp*0.2 [MPa]	*Rm* [MPa]	*At* [%]
0°	183 ± 15.58	917 ± 9.9	1263 ± 8.6	11.1 ± 1.14
30°	148 ± 20.57	965 ± 5.9	1272 ± 10.3	10.4 ± 1.31
60°	167 ± 26.23	845 ± 11.1	1247 ± 6.1	17.1 ± 1.35
90°	139 ± 6.93	755 ± 8.7	1188 ± 6.3	24.3 ± 0.70
Average	159	871	1243	15.7

Table 2. Tensile properties of Co–Cr–W in the heat treated condition; extracted from [20]. Φ : Inclination, *E*: Young's modulus, *Rp*0.2: Yield strength, *Rm*: Ultimate tensile strength, *At*: Elongation at failure.

Φ [°]	*E* [GPa]	*Rp*0.2 [MPa]	*Rm* [MPa]	*At* [%]
0°	216 ± 21.99	655 ± 26.6	1111 ± 8.9	15.0 ± 1.54
30°	187 ± 7.90	651 ± 4.9	1127 ± 12.3	15.5 ± 1.04
60°	215 ± 29.25	669 ± 20.0	1162 ± 13.4	18.0 ± 2.90
90°	202 ± 22.08	658 ± 7.1	1108 ± 10.9	16.9 ± 1.51
Average	205	658	1127	16.4

3.3 XRD

XRD experiments verified an fcc matrix, a stress induced transformation to the hexagonal ε-phase (observed e. g. via the reflection at observed at $\theta \approx 47°$), and one or more additional phases, evidenced by the reflections at $2\theta \approx 45°$ in Figure 4(b). These reflections were evident in both heat treated states, while the ε-phase was only present in both deformed states. Hence, plastic deformation and the heat treatment described in section 2.1 promote distinct phases.

3.4 Focused Ion Beam and Scanning Electron Microscopy (FIBSEM)

Inverse pole Figures 5(a) and 5(b) display comparable grain sizes for both investigated states and recrystallisation or annealing twins in the heat treated state. The orientation deviation maps 5(c) and 5(d) show the deviation of the local Kikuchi pattern from the grain's average orientation. The abundance of green and yellow areas in the initial state indicates a larger amount of residual (intragranular) strains, resulting from the thermomechanical loading during the LPBF process. The annealing occuring during heat treatment results in a reduction of the orientation deviations within the heat treated state. EDS measurements reveal strong differences in the tungsten concentrations (see Figure 6). With appropriate spectrum fitting, the material was characterised as being comprised of two components, namely a matrix phase and a precipitate phase. The Si concentrations were not clearly observable due to overlap with the tungsten L-line. The varying tungsten concentrations were a further indicator for a precipitated phase.

3.5 TEM

More finely resolved EDS measurements of the heat treated state were performed (see Figure 7). In addition to the expected elements, approximately 2 at. % of Nb and difficult to quantify amounts of O and Si were found. As the EDS spectra of the precipitates were similar to each other, differing mainly in their tungsten concentrations from the matrix (see Figure 6), the following quantitative evaluation was limited and renormalized to three elements. Averaging the chemical concentrations over three areas within precipitates resulted in $c_{Cr} = 21.34$ at %, $c_{Co} = 49.58$ at. % and $c_W = 28.21$ at. %. The only crystal structure capable of describing all found diffraction patterns was the D024-structure (see Figures 8b

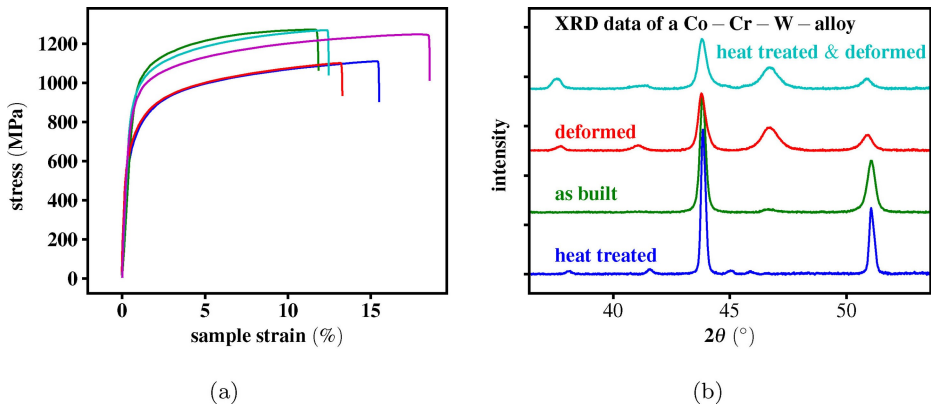

Figure 4. 4a: Exemplary data of five randomly selected tensile experiments, adapted from [20]. The green, cyan and magenta datasets stem from as-built specimens, while the blue and red curves stem from the heat treated condition. 4b: Intensity (arbitrary units) over 2θ of the as-build and the heat treated conditions, respectively, in the post mortem tensile tested and the initial states.

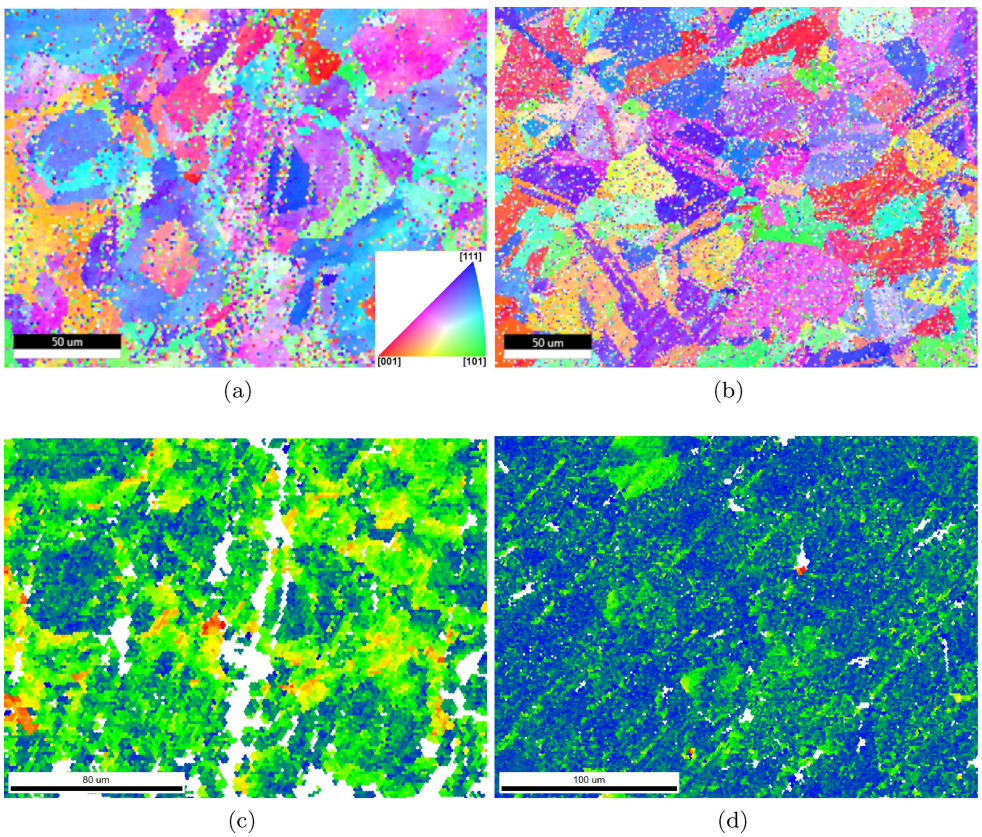

Figure 5. Results of EBSD measurements for the initial state (5a 5c) and the heat treated state (5b 5d). For these large scans, identifying Kikuchi patterns of small precipitates was abstained from. 5a and 5b: Inverse pole Figures. 5c and 5d: Intragranular misorientations.

and 8a for exemplary diffraction patterns). Further phases fulfilling the 3 : 1 stoichiometry, like the L12-, the D019- and the D022- structure were considered, but none of these were able to match the data.

4. Discussion

In contrast to previous studies,[20] XRD measurements showed varying responses to tensile deformation and heat treatment, with the ε-phase only being present after plastic deformation. The stress induced phase transformation may contribute to the

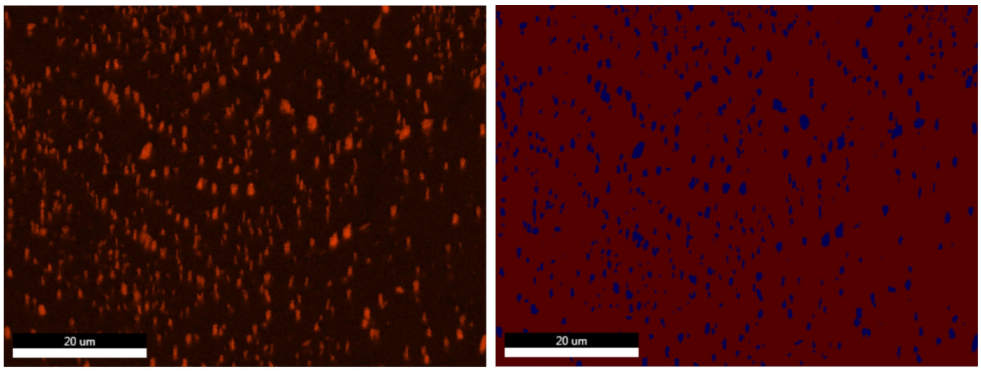

(a) (b)

Figure 6. EDS maps of a specimen in the heat treated condition. 6a: EDS-Mapping of the tungsten M-line. 6b: Phase mapping from the same area, showcasing a tungsten- rich phase (blue).

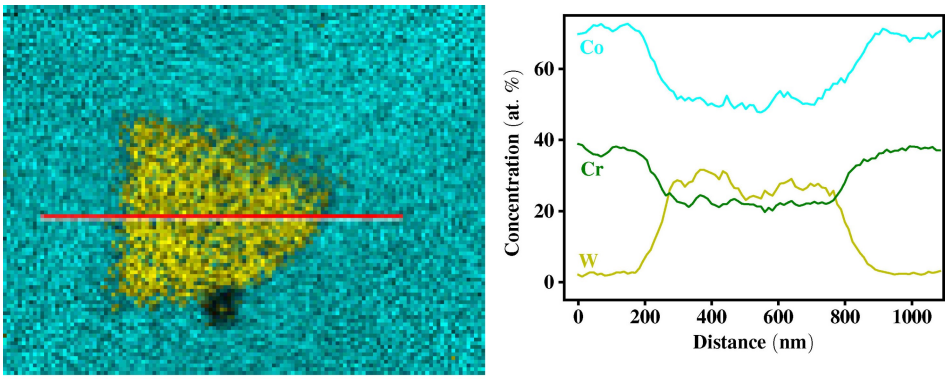

(a) (b)

Figure 7. 7a: EDS map aquired in transmission geometry. The red path marks the line for the scan in 7b. A quantitative evaluation yields c_{Cr} = 21.34 at. %, c_{Co} = 49.58 at. % and c_{W} = 28.21 at. %. This is interpreted as a precipitated phase with the stoichiometry $(Co, Cr)_3W$.

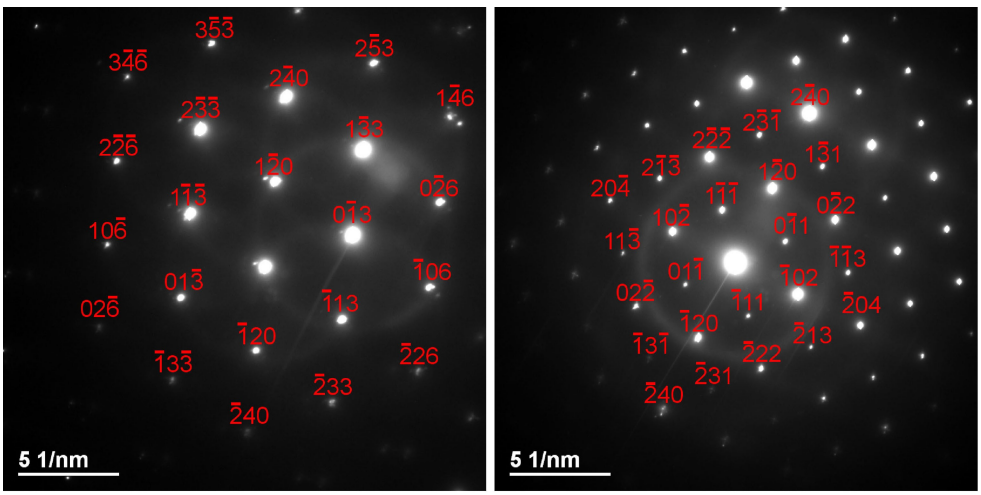

(a) (b)

Figure 8. Exemplary electron diffraction patterns of two precipitates, indexed with the D024-phase. 8a: precipitate close to the [6 3 1]- zone axis. 8b: precipitate close to the [2 1 1]- zone axis.

aforementioned (see section 3.2) work hardening.[27] Further, analyses by electron microscopy showed that the phase formation caused by heat treatment was related to chemical inhomogeneities. These microstructural changes require diffusion and cannot be purely caused by a stress induced phase transformation. The prospect of a phase transformation during plastic deformation may change the precipitation during post heat treatments. EDS measurements in the FIBSEM resulted in a precipitate volume fraction of ~7–10%, while predictions based on the stoichiometry $(Co, Cr)_3W$ result in a theoretical maximum of 12%. Based on this estimation, together with the formation of these precipitates being the major change regarding present phases in the tested samples prior to deformation (Figure 4(b)), it remains to be seen whether or not their presence can explain the significant gain in the elastic stiffness among the two tested configurations. Two common estimates for the upper and lower bounds of the Young's moduli of composite materials are a linear and an inverse law of mixture:[28]

$$E_c^{linear} = V_A E_A + V_B E_B \quad (1)$$

$$E_c^{inverse} = \frac{E_A E_B}{V_A E_B + V_B E_A} \quad (2)$$

These respective expressions represent models (depending on assumed homogeneous strain and stress, respectively) and are often considered upper and lower bounds of the elastic constants of fiber or particulate composites. Assuming the average Young's modulus of the γ-matrix to stay the same as in the as-built condition ($E_A = 159$ GPa), allows, for a given volume fraction of the precipitates, to estimate the Young's modulus of the precipitated phase by setting $E_c = 205$ GPa.

For the range between 10% and 40% precipitate phase, the calculated Young's moduli are shown in Figure 9. Values above 600 GPa are not considered as meaningful results and are not shown here. It is evident, that the inverse rule of mixture results in an overestimate of the Young's modulus of tungsten-rich precipitates. In contrast, a linear rule of mixture could approach plausibility, even though the predicted Young's modulus of 542 GPa was still very high. For comparison, the elastic properties estimated on the basis of density functional theory for different phases with the stoichiometry Co_3W are propagated via homogenization schemes to Young's moduli.[29–31] For the phase of D019-structure described in mp-2157,[32] this leads to 369 GPa (Voigt), 356 GPa (Reuss), and 364 GPa (Hill). For the phase of L12-structure described in mp-1008274,[33] this yields 392 GPa (Voigt), 364 GPa (Reuss), and 378 GPa (Hill). Overall, the increase in Young's moduli can only partially be attributed to phase transformations. More elusive explanations should be considered, e.g. residual stresses contributing to plastic deformations even at small macroscopic stresses making Young's moduli seem smaller. Typically, the D019-phase is a more stable configuration of Co_3W than the D024-phase.[34] However, as in the related Nickel-based superalloys creep conditions promote the D024 structure, formation of this phase in these specimens, which are rich in inter- and intragranular stresses, seems plausible.[35]

5. Conclusions

Plastic deformations of LPBF manufactured Remanium star CL alloy specimens were associated to a stress induced formation of the hexagonal ε-phase in both the heat treated and the initial state. The material was shown to precipitate the intermetallic D024-phase during its recommended heat treatment, which can partially explain the observed increase of its Young's modulus. Further mechanical studies on the elastic behaviour of the as build state during unloading promise additional insights. Concerning dental applications, the precipitation of tungsten implies the possibility of finely dispersed local electrochemical elements, adversely influencing the corrosive behaviour when in contact with saliva.

Acknowledgements

We gratefully acknowledge the DFG for funding this research within Project 280883331. Further, we wish to thank Objective3D and Dr. F. Alifui-Segbaya for supplying samples.

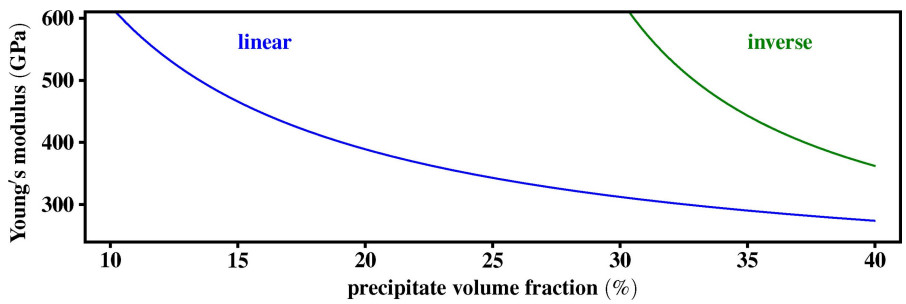

Figure 9. Estimation of the Young's modulus of the precipitates via two different laws of mixture.

References

[1] L. Hitzler, M. Merkel, W. Hall, A. Öchsner, *Adv. Eng. Mater.* **2018**, *20*, 1700658.
[2] L. Hitzler, PhD thesis, (Griffith Univ., Griffith School of Engineering and Built Environment, Gold Coast, AUS, **2018**.
[3] ISO/ASTM 52900 (2015), Standard Terminology for Additive ManufacturingGeneral PrinciplesTerminology.
[4] F. Mangano, L. Chambrone, R. Van Noort, C. Miller, P. Hatton, C. Mangano, *Int. J. Biomat.* **2014**, *2014*, 461534.
[5] J. P. Kruth, B. Vandenbroucke, J. Van Vaerenbergh, I. Naert, *Journal of Dental Technology* **2007**, 24–32.
[6] L. Murr, *Mater. Technol.* **2018**, *33*, 57–70.
[7] M. Koike, P. Greer, K. Owen, G. Lilly, L. E. Murr, S. M. Gaytan, E. Martinez, T. Okabe, *Materials* **2011**, *4*, 1776–1792.
[8] B. Vandenbroucke, J.-P. Kruth, *Rapid Prototyping Journal* **2007**, *13*, 196–203.
[9] D. Jevremovic, T. Puskar, B. Kosec, Đ. Vukelic, I. Budak, S. Aleksandrovic, D. Egbeer, R. Williams, *Metalurgija* **2012**, *51*, 171.
[10] F. Alifui-Segbaya, P. Foley, R. J. Williams, *Rapid Prototyping Journal* **2013**, *19*, 95–99.
[11] T. Puskar, D. Jevremovic, R. Williams, D. Eggbeer, D. Vukelic, I. Budak, *Materials* **2014**, 7, 6486–6501.
[12] D. Jevremovic, V. Kojic, G. Bogdanovic, T. Puskar, D. Eggbeer, D. Thomas, R. Williams, *Ser. Chem.* **2011**, *76*, 43–52.
[13] T. Puskar, A. Lapcevic, S. Arandjelovic, S. Radulovic, I. Budak, D. Vukelic, D. Jevremovic, *Metalurgija* **2015**, *54*, 481–484.
[14] F. Alifui-Segbaya, R. J. Williams, R. George, *J. Prosthet. Dent.* **2017**, *25*, 73–78.
[15] Food and Drug Administration, D. *Technical Considerations for Additive Manufactured Devices:Draft Guidance for Industry and Food and Drug Administration Staff*, **2016**, p. 28.
[16] L. Hitzler, J. Hirsch, B. Heine, M. Merkel, W. Hall, A. Öchsner, *Materials* **2017**, *10*, 1136.
[17] L. Hitzler, C. Janousch, J. Schanz, M. Merkel, B. Heine, F. Mack, W. Hall, A. Öchsner, *J. Mater. Process. Technol.* **2017**, *243*, 48–61.
[18] F. Alifui-Segbaya, J. Evans, D. Eggbeer, R. George, *Proceedings of the 1st International Conference on Progress in Additive Manufacturing (Pro-AM 2014)* **2014**, 115–120.
[19] N. Xiang, X. Z. Xin, J. Chen, B. Wei, *J. Dent.* **2012**, *40*, 453–457.
[20] L. Hitzler, F. Alifui-Segbaya, P. Williams, M. Merkel, B. Heine, M. Heitzmann, W. Hall, A. Öchsner, *Adv. Mater.* **2018**, *2018*, 8213023.
[21] Y. Kajima, A. Takaichi, N. Kittikundecha, T. Nakamoto, T. Kimura, N. Nomura, A. Kawasaki, T. Hanawa, H. Takahashi, N. Wakabayashi, *Mater. Sci. Eng. A* **2018**, *726*, 21–31.
[22] S. Y. Yang, M. Jiang, H. X. Li, L. Wang, *Trans. Nonferrous Met. Soc. China* **2011**, *21*, 2270–2275.
[23] B. S. Institute, BS ISO 22674: 2006: Dentistry-Metallic Materials for Fixed and Removable Restorations and Appliances, **2006**.
[24] DIN, ENISO, 6892 Teil 1, **2009**.
[25] P. Stadelmann, *Microsc. Microanal.* **2003**, *9*, 60–61.
[26] S. Gorsse, C. Hutchinson, M. Gouné, R. Banerjee, *Sci. Technol. Adv. Mater.* **2017**, *18*, 584–610.
[27] X. Wu, N. Tao, Y. Hong, J. Lu, K. Lu, *Scr. Mater.* **2005**, *52*, 547–551.
[28] E. Hornbogen, G. Eggeler, E. Werner, *Werkstoffe*, 12th ed., Springer, **2019**, p. 420.
[29] A. Jain, S. P. Ong, G. Hautier, W. Chen, W. D. Richards, S. Dacek, S. Cholia, D. Gunter, D. Skinner, G. Ceder, K. A. Persson, *APL Materials* **2013**, 1, 011002.
[30] M. de Jong, W. Chen, T. Angsten, A. Jain, R. Notestine, A. Gamst, M. Sluiter, C. Krishna Ande, S. van der Zwaag, J. J. Plata, C. Toher, S. Curtarolo, G. Ceder, K. A. Persson, M. Asta, *Scientic Data* **2015**, 2, DOI10.1038/sdata.2015.9.
[31] R. Gaillac, P. Pullumbi, F.-X. Coudert, *J. Phys. Condens. Matter* **2016**, *28*, 275201.
[32] K. A. Persson, **2016**, DOI 10.17188/1197003.
[33] K. Persson, **2016**, DOI 10.17188/1325022.
[34] K. Vamsi, S. Karthikeyan, *Scr. Mater.* **2017**, *130*, 269–273.
[35] P. Kontis, A. Kostka, D. Raabe, B. Gault, *Acta Mater.* **2019**, *166*, 158–167.

Manuscript received: November 28, 2019
Revised manuscript received: January 22, 2020
Version of record online: March 9, 2020

